WILEY-VCH

Supporting Information

Long-range cation disorder enhances comprehensive performance in Mn-rich layered sodium cathodes

Maolin Yang, Tingting Yang, Mingjie Dong, Zhongyuan Huang, Yuguang Pu, Lei Jin, Rui Wang, Yuxi Luo, Tao Zeng, Yonglin Tang, Jun Chen, Rafal E. Dunin-Borkowski, Ziwei Chen, Yu Qiao, Yinguo Xiao**

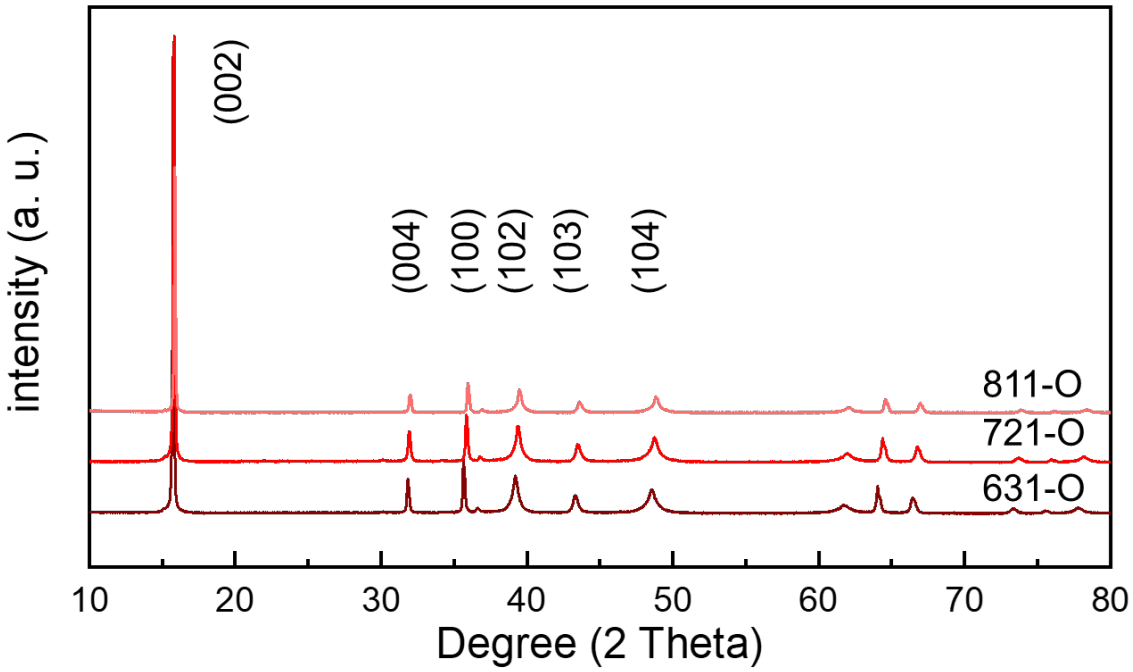

Figure S1. XRD patterns of as synthetized samples.

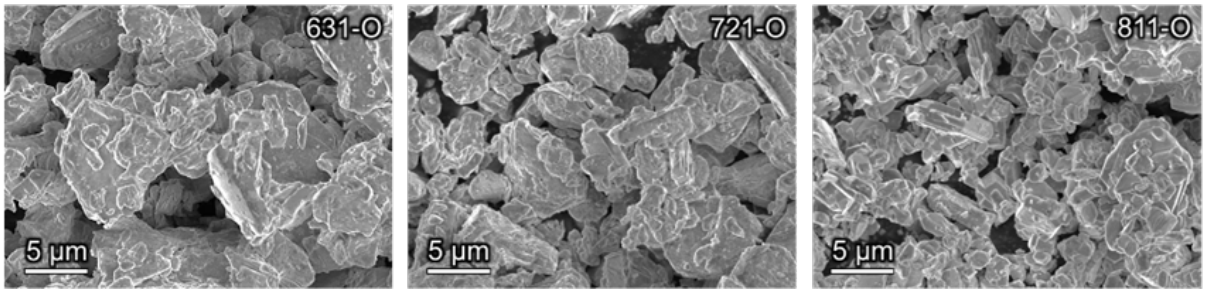

Figure S2. SEM images of as synthetized samples.

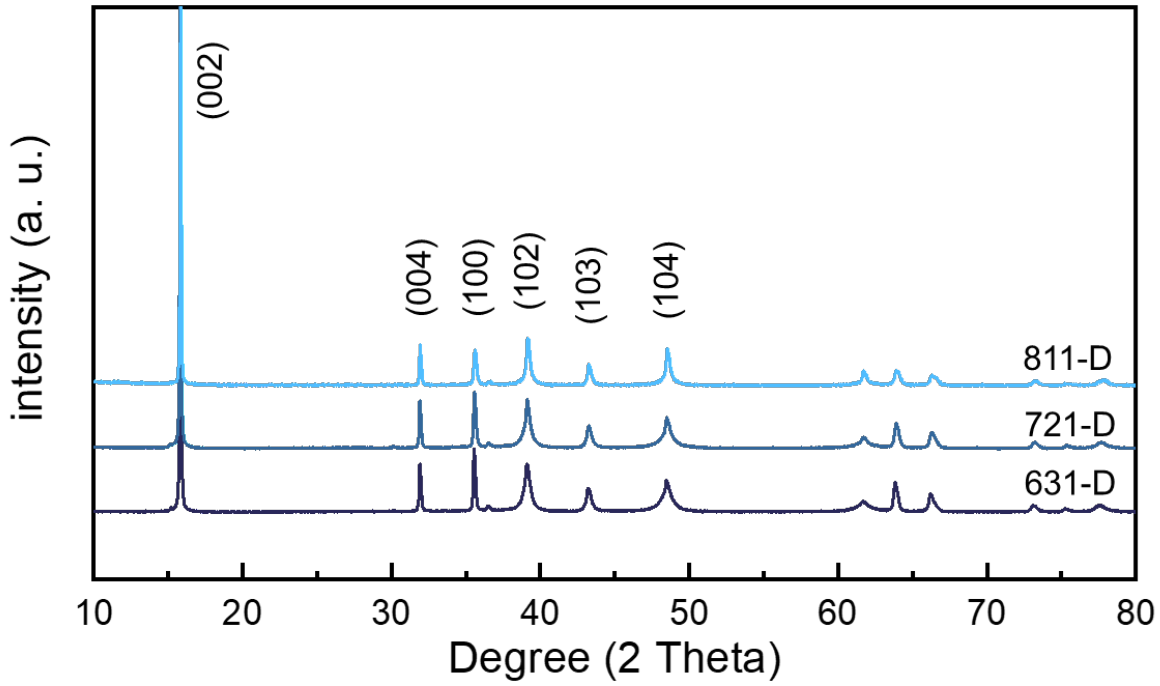

Figure S3. XRD patterns of the modified samples.

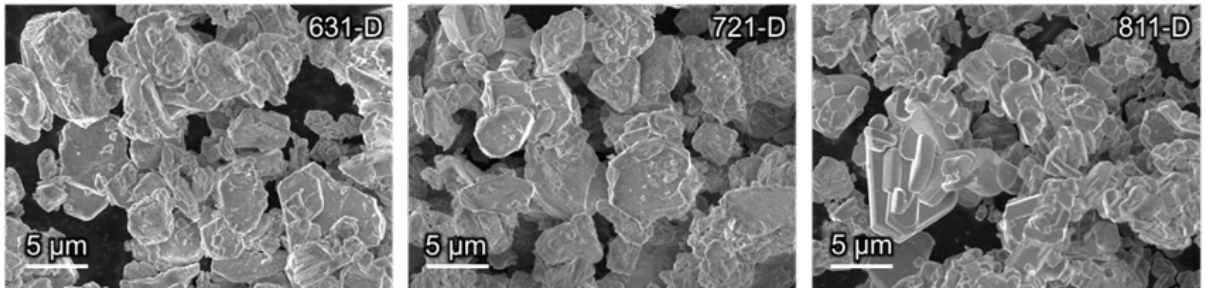

Figure S4. SEM images of the modified samples.

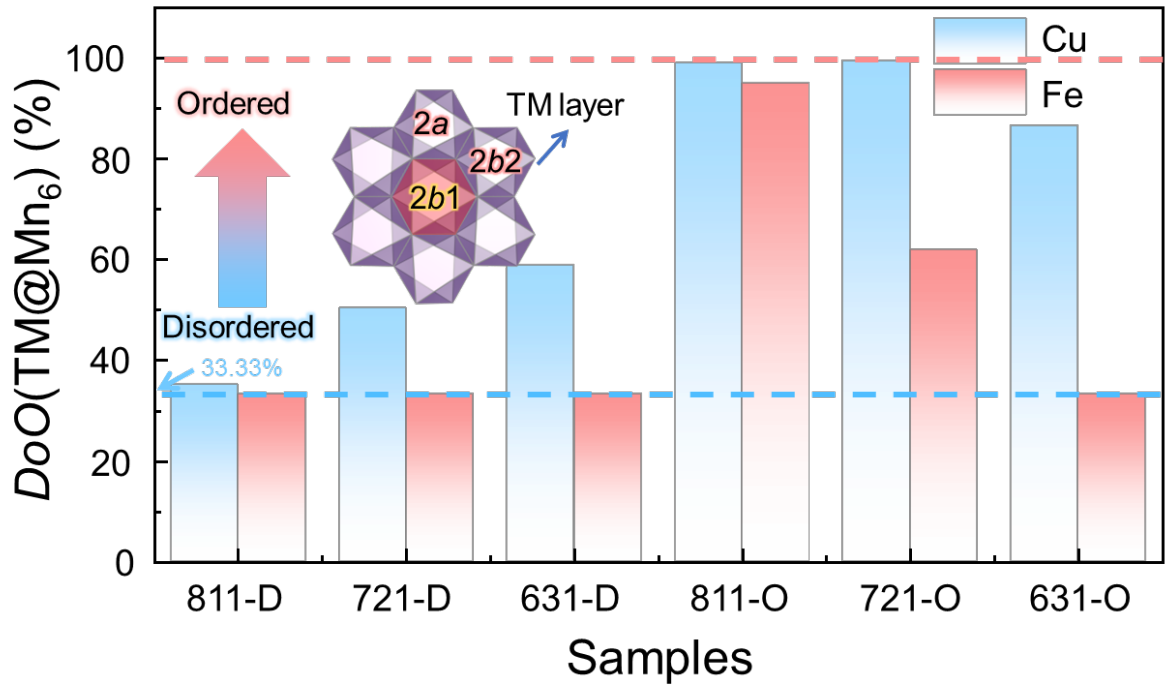

Figure S5. Calculated *DoO*(TM@Mn_6) of as-synthesized samples (TM=Cu or Fe, located at TM_{2b1} site), all the refinement results were based on a *P6₃* symmetry. The inset illustrates the three TM ionic sites within the honeycomb superstructure, which are classified into three distinct types: TM_{2a}, TM_{2b1}, and TM_{2b2}.

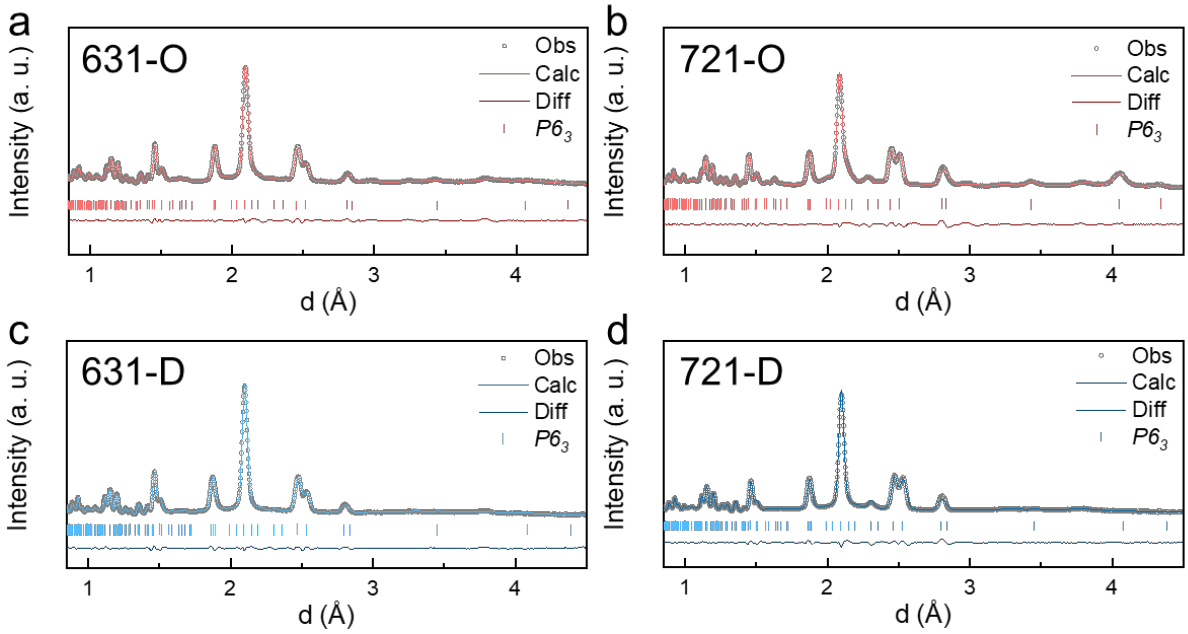

Figure S6. (a-d) Rietveld NPD refinement results of (a) 631-O, (b) 721-O, (c) 631-D and (d) 721-D.

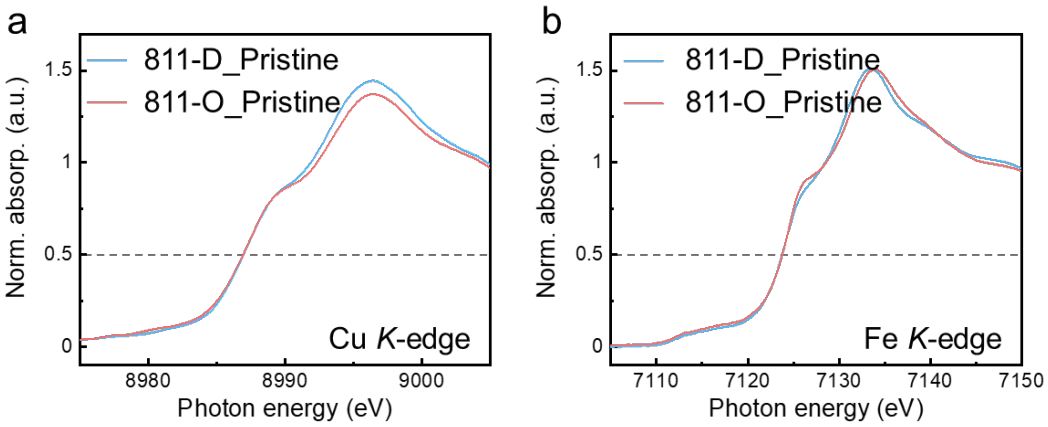

Figure S7. (a, b) Normalized (a) Cu *K*-edge and (b) Fe *K*-edge XANES spectra of 811-O, 811-D at pristine state.

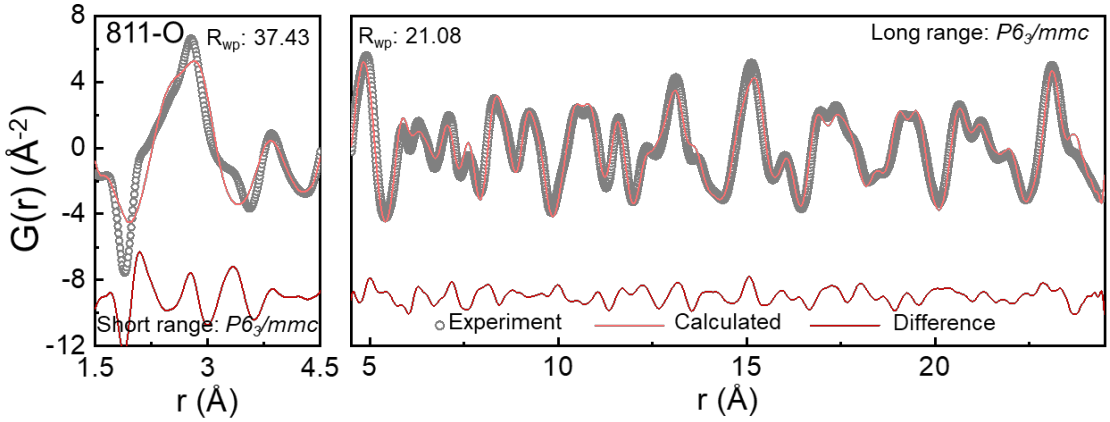

Figure S8. Refinement results of nPDF for 811-O within short-range with *P6₃/mmc* symmetry and long-range with *P6₃/mmc* symmetry.

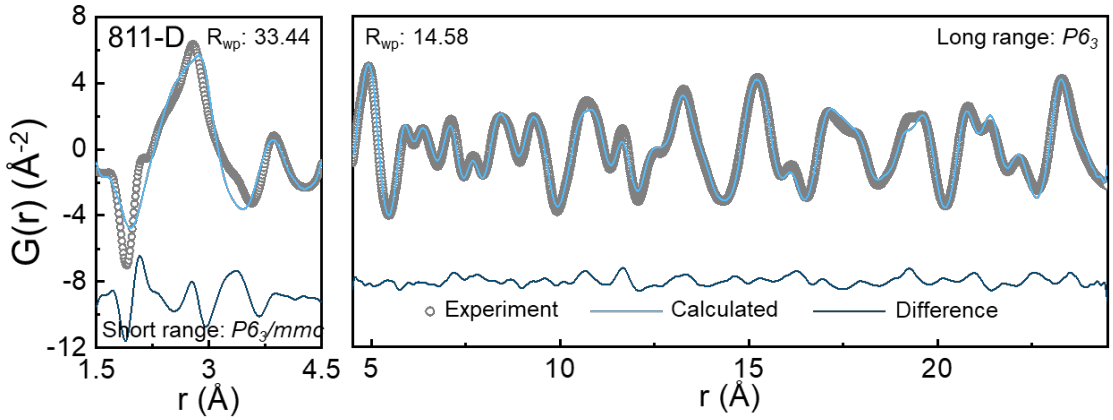

Figure S9. Refinement results of nPDF for 811-D within short-range with *P6₃/mmc* symmetry and long-range with *P6₃* symmetry.

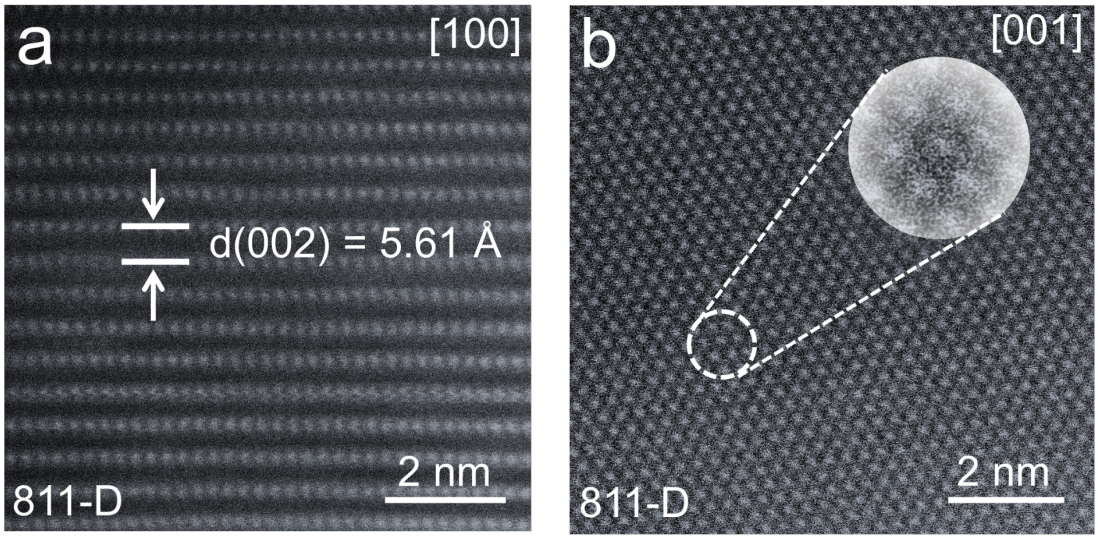

Figure S10. (a, b) STEM-HAADF images of 811-D along (a) [100] and (b) [001] zone axis.

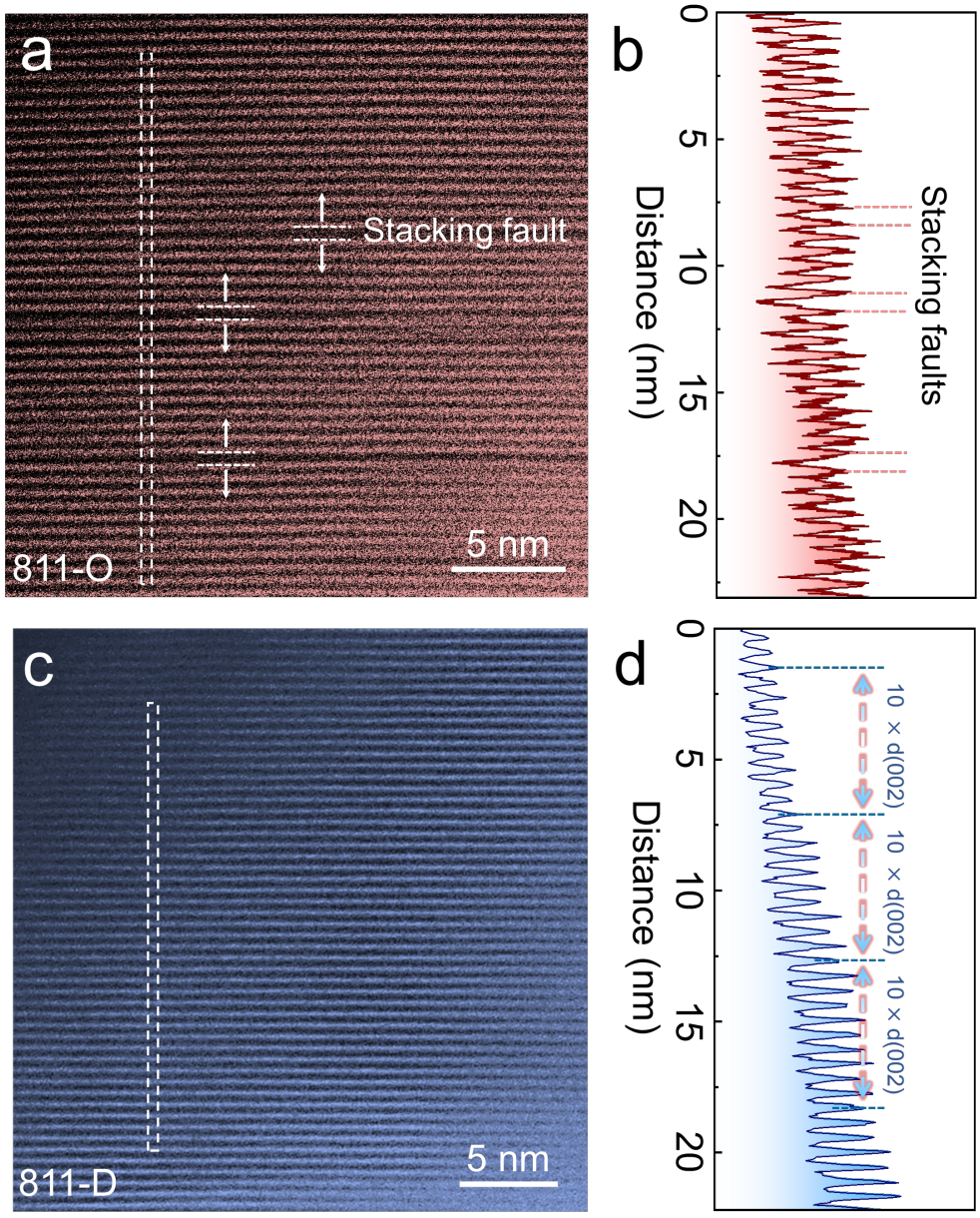

Figure S11. (a) STEM-HAADF image of 811-O along [100] zone axis; (b) Line scan profile along the corresponding rectangle in (a); (c) STEM-HAADF image of 811-D along [100] zone axis; (d) Line scan profile along the corresponding rectangle in (c);

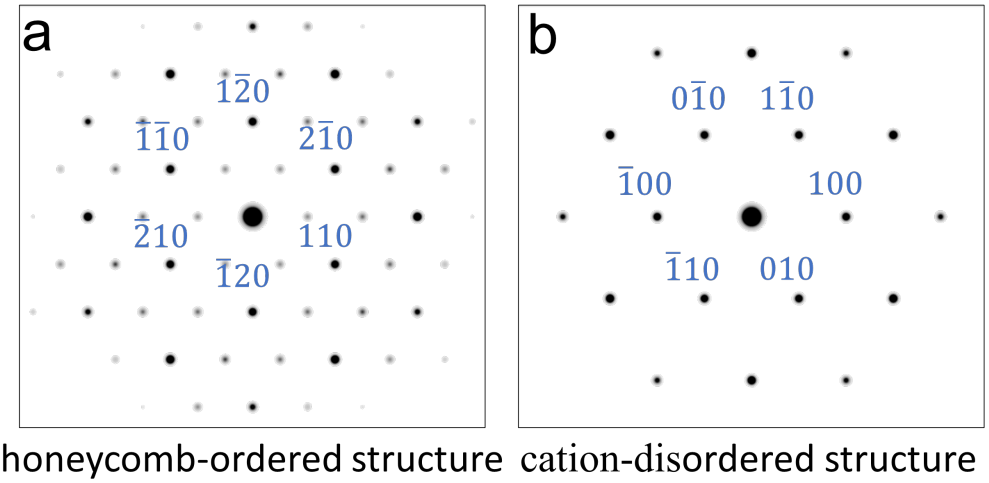

Figure S12. (a, b) Simulated electron diffraction patterns along the [001] zone axis of (a) honeycomb-ordered structure and (b) cation-disordered structure.

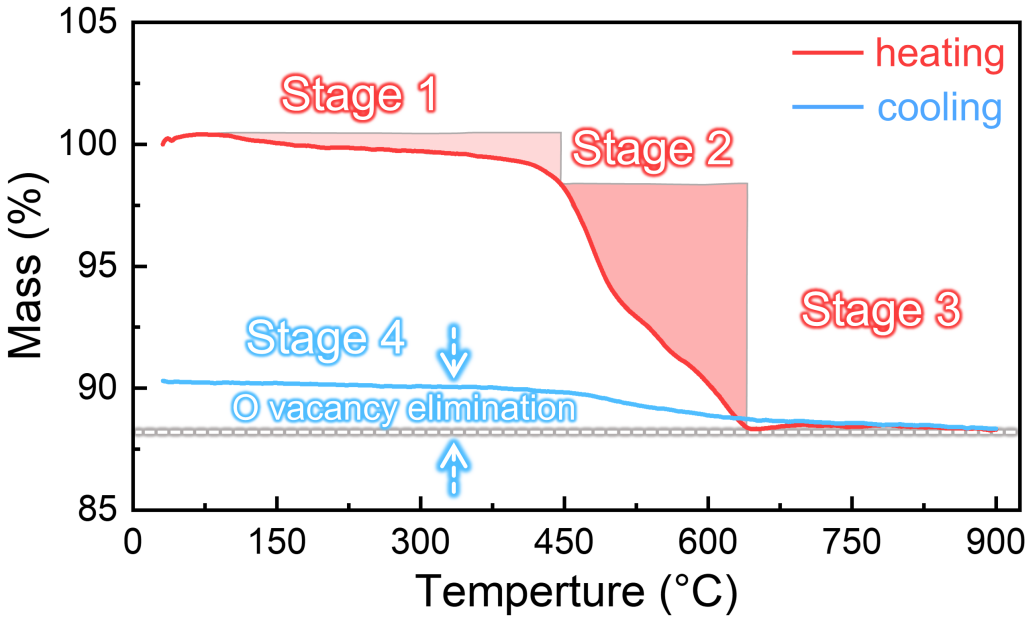

Figure S13. TGA measurement during the simulation of the synthesis process of 811-O.

Figure S13 displays the TGA analysis during the solid-state synthesis of 811-O using TM oxides and Na_2CO_3 as reactants. The red line represents the heating process, the blue line denotes the cooling process, and the gray dashed line serves as a guide. Based on the weight loss profile, the heating process can be divided into three stages: stage 1 corresponds to water removal; stage 2 to carbonate decomposition; and stage 3 to the calcination and formation of the layered material, consistent with literature reports.[1] Notably, an increase in weight during the cooling process indicates oxygen uptake by the lattice, signifying the elimination of oxygen vacancies.[2]

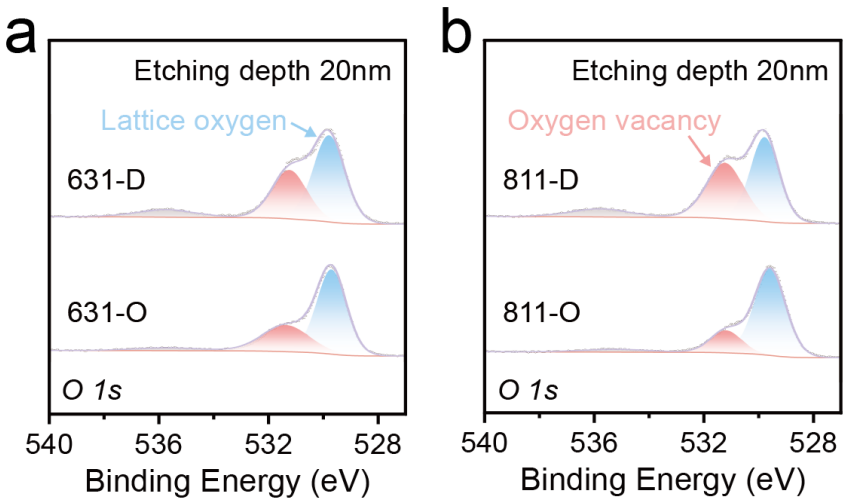

Figure S14. (a, b) O *1s* XPS spectra of (a) 631-O, 631-D, (b) 811-O and 811-D at the etched depth of 20 nm.

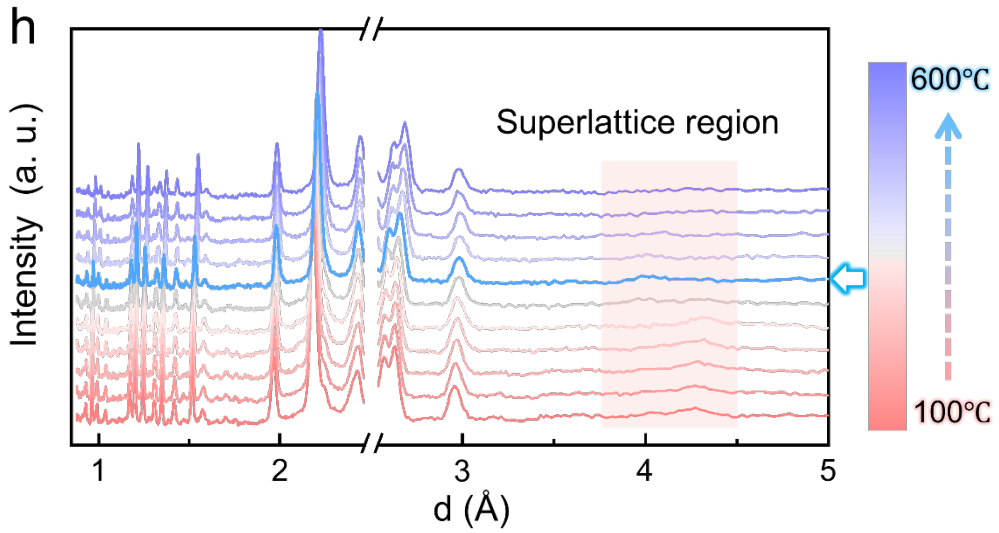

Figure S15. Raw data of in situ neutron diffraction experiment of 811-O during heating process. The data were collected from 100 °C to 600 °C in increments of 50 °C from bottom to top, with the blue-highlighted data indicated by the arrow representing the NPD data measured at 400 °C.

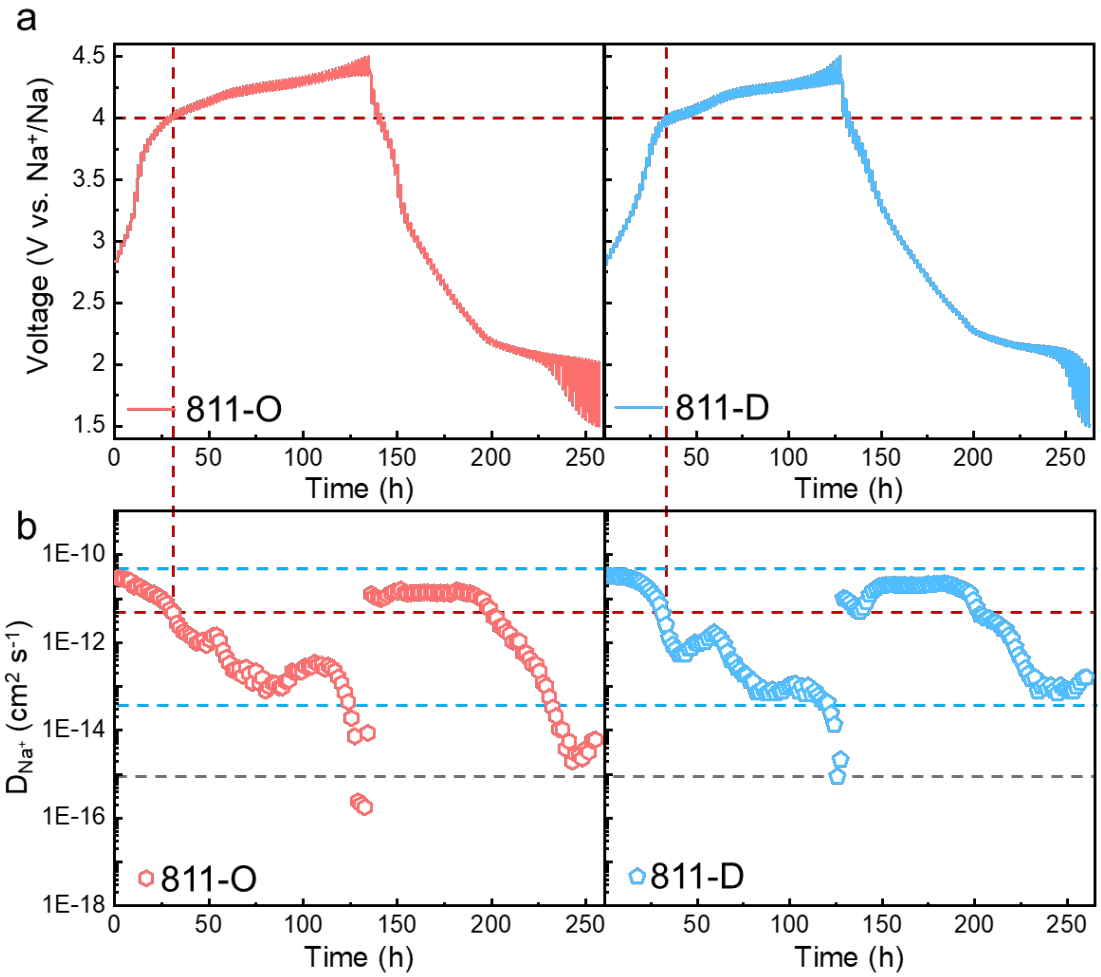

Figure S16. (a) GITT curves of 811-O and 811-D at initial cycle within 1.5–4.5 V. (b) Corresponding D_{Na^+} calculated via GITT tests.

Figure S16a shows that during the charging process from OCV to 4 V, both 811-O and 811-D exhibit a ramp-type charging curve, with both samples displaying relatively high D_{Na^+} (Figure S16b). As charging progresses to higher voltages, a pronounced plateau emerges in both samples, typically indicating a P2–OP4 phase transition accompanied by oxygen oxidation reactions.[3] At this stage, the narrowing of the Na layer due to the phase transition and the sluggish kinetics of the anionic oxidation reaction lead to a sudden decrease in D_{Na^+}. Notably, although 811-D has a lower residual sodium content than 811-O at 4.5 V (0.10 mol vs. 0.19 mol), it still maintains a higher D_{Na^+}. Furthermore, during discharge, the D_{Na^+} of 811-D consistently exceeds that of 811-O, further confirming that cation disordering enhances Na^+ diffusion kinetics in layered cathode materials.

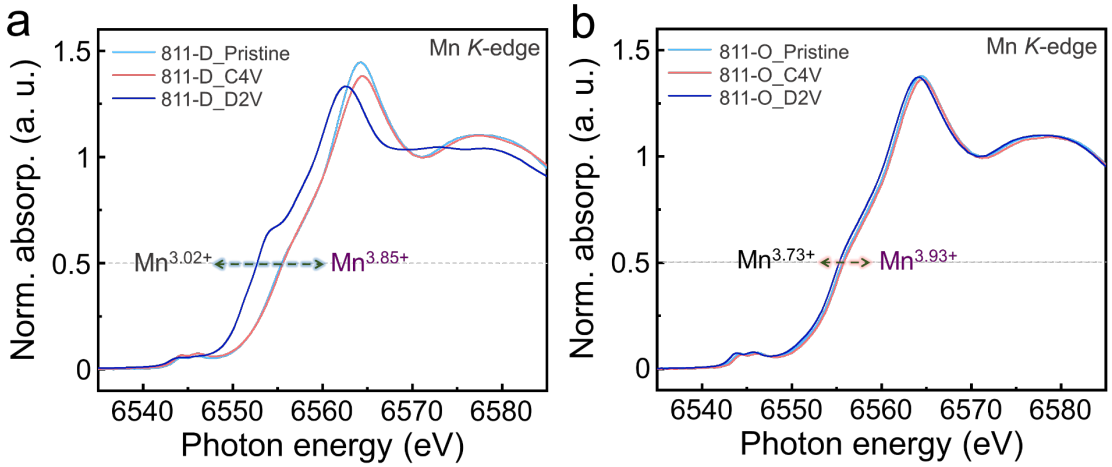

Figure S17. (a, b) Normalized Mn *K*-edge XANES at various charged/discharged states of 811-D (a) and 811-O (b).

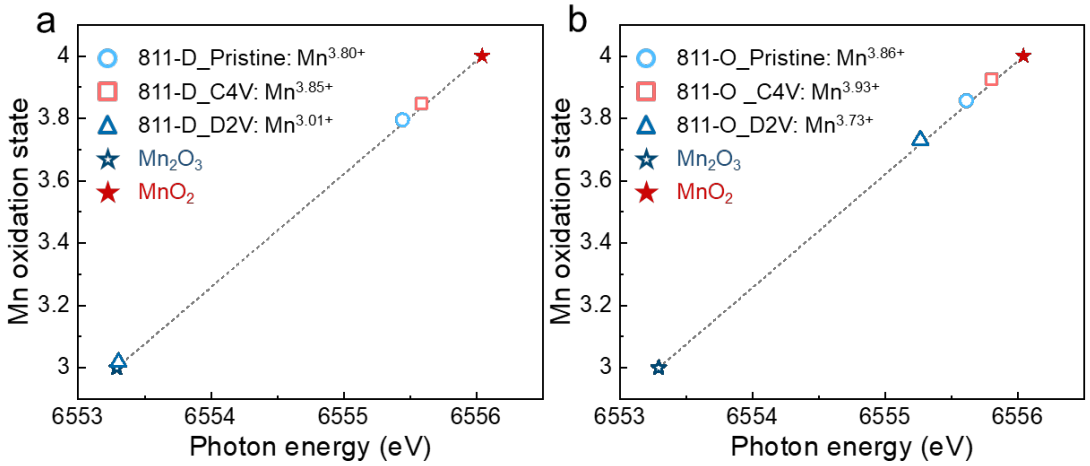

Figure S18. (a, b) Mn valence evolutions of (a) 811-D and (b) 811-O are quantificationally analyzed by the integration method with the Mn_2O_3, and MnO_2 reference data.[4]

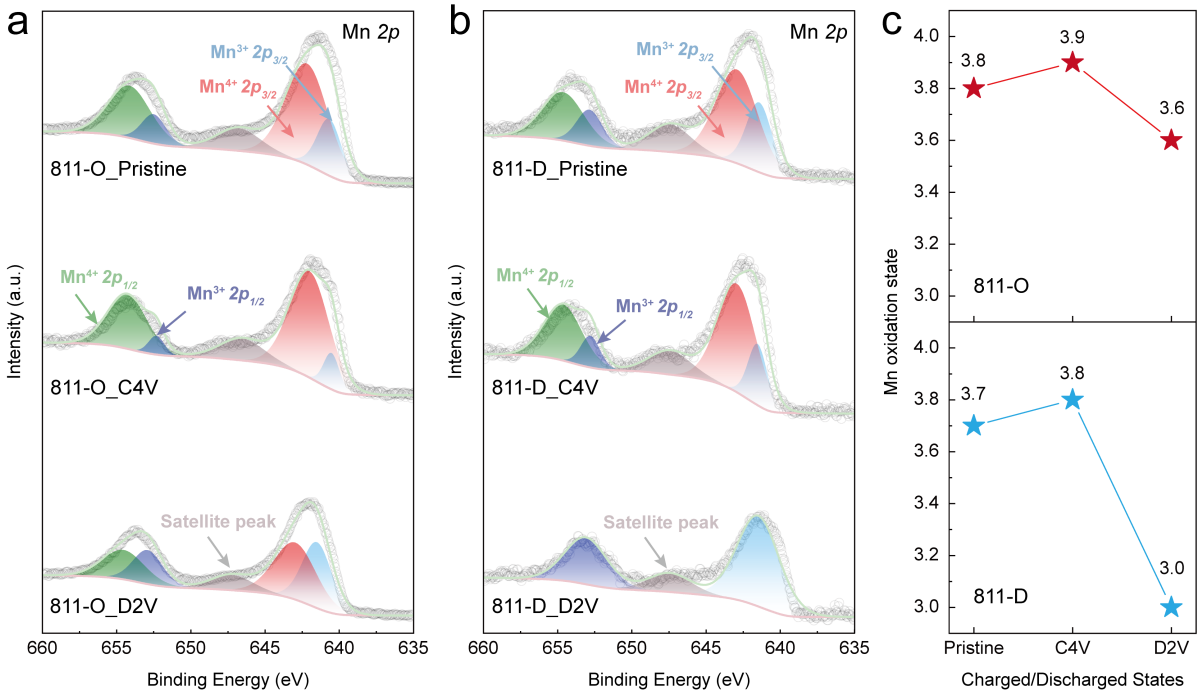

Figure S19. (a, b) Ex situ Mn *2p* XPS spectra of (a) 811-D and (b) 811-O at the etched depth of 20 nm. (c) The calculated Mn valence at various charged/discharged states of 811-O and 811-D base on their integral area in (a, b).

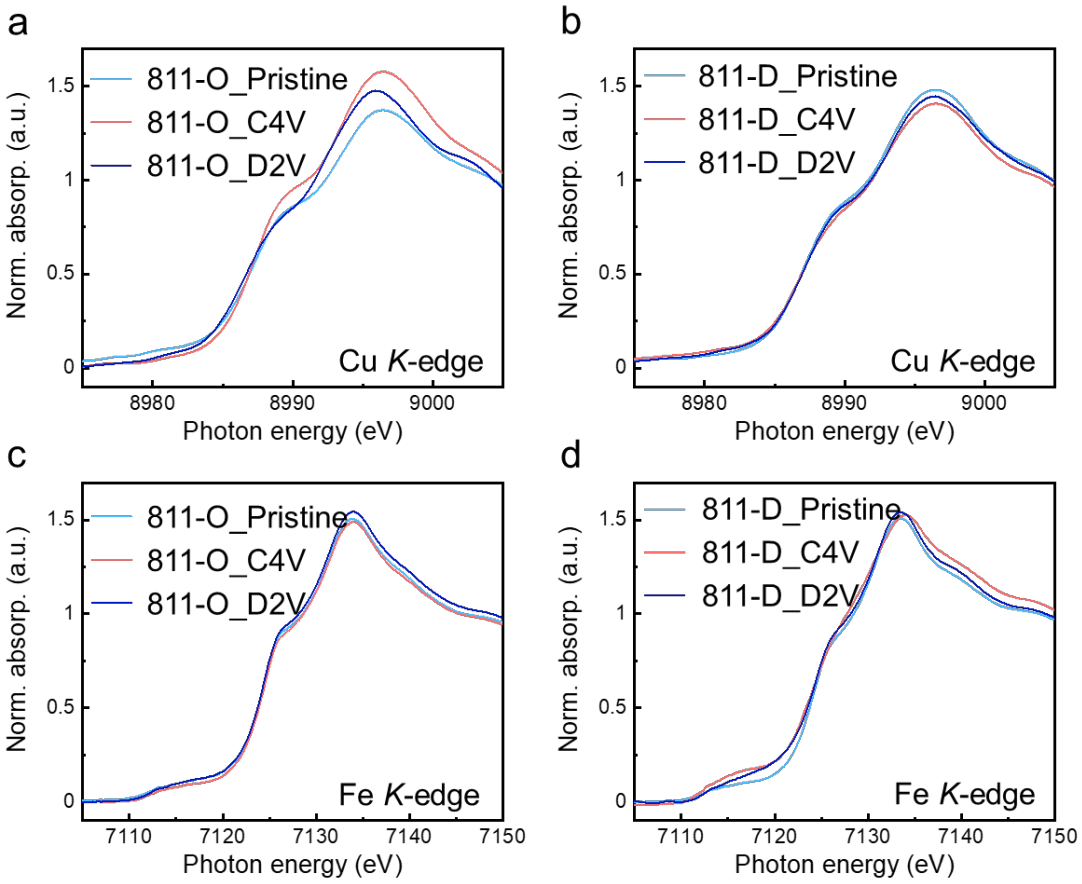

Figure S20. (a, b) Normalized Cu *K*-edge XANES at various charged/discharged states of (a) 811-O and (b) 811-D. (c, d) Normalized Fe *K*-edge XANES at various charged/discharged states of (c) 811-O and (d) 811-D.

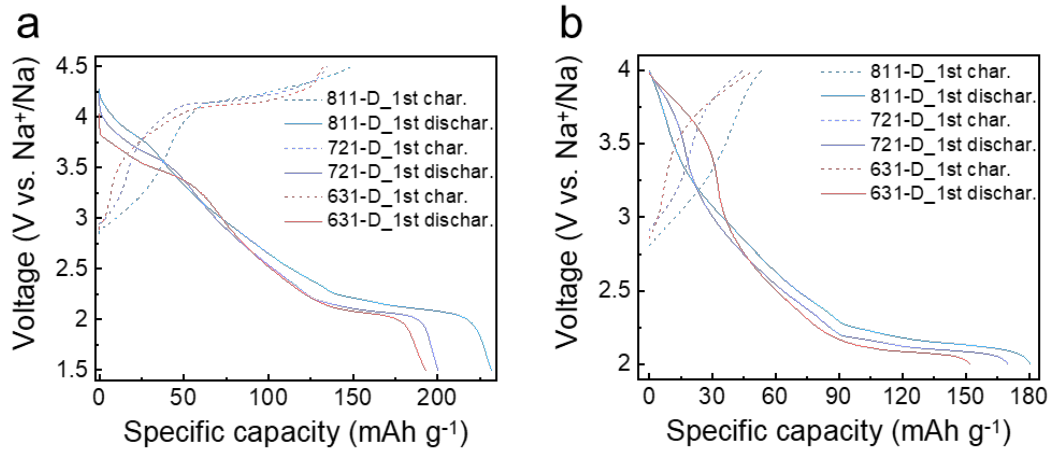

Figure S21. (a, b) Typical GCD curves of 811-D, 721-D and 631-D during the first cycle within (a) 1.5–4.5 V and (b) 2–4 V.

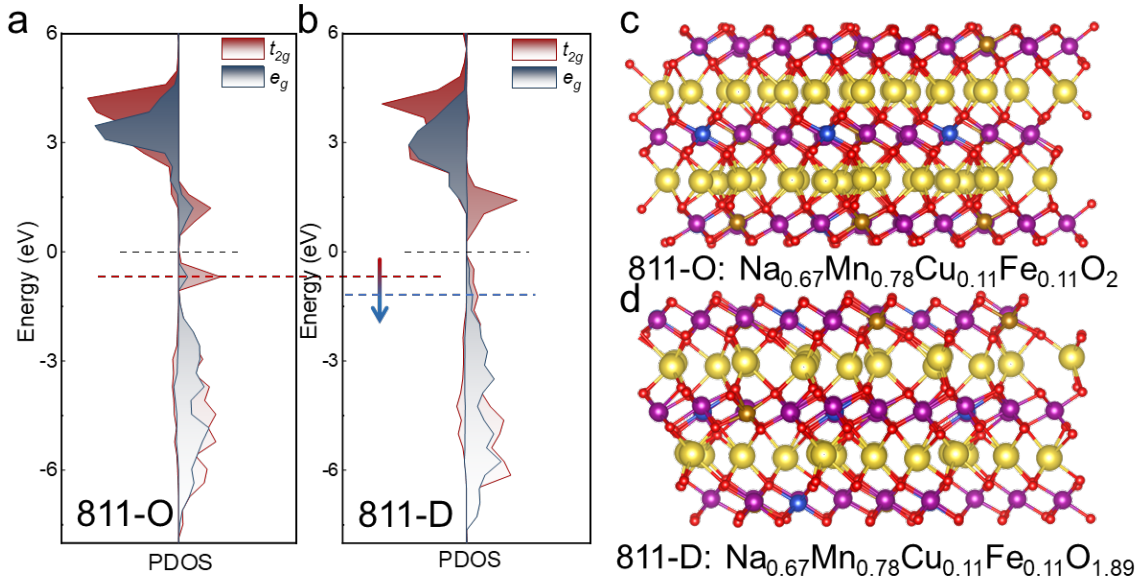

Figure S22. (a, b) Projected DOS of the Mn *3d* orbitals in (a) 811-O and (b) 811-D. (c, d) The theoretically most stable supercell structure of (c) 811-O without bulk Vo and (d) 811-D with bulk Vo.

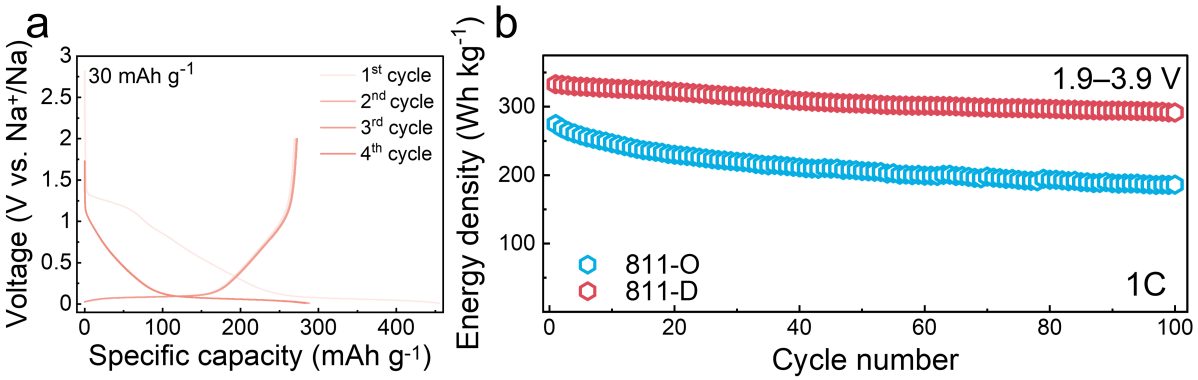

Figure S23. (a) GCD curves at 50 mA g^{-1} for the first four cycles of hard carbon (HC). (b) The long-term cycling energy densities of 811-O||HC and 811-D||HC at 1C within 1.9-3.9 V.

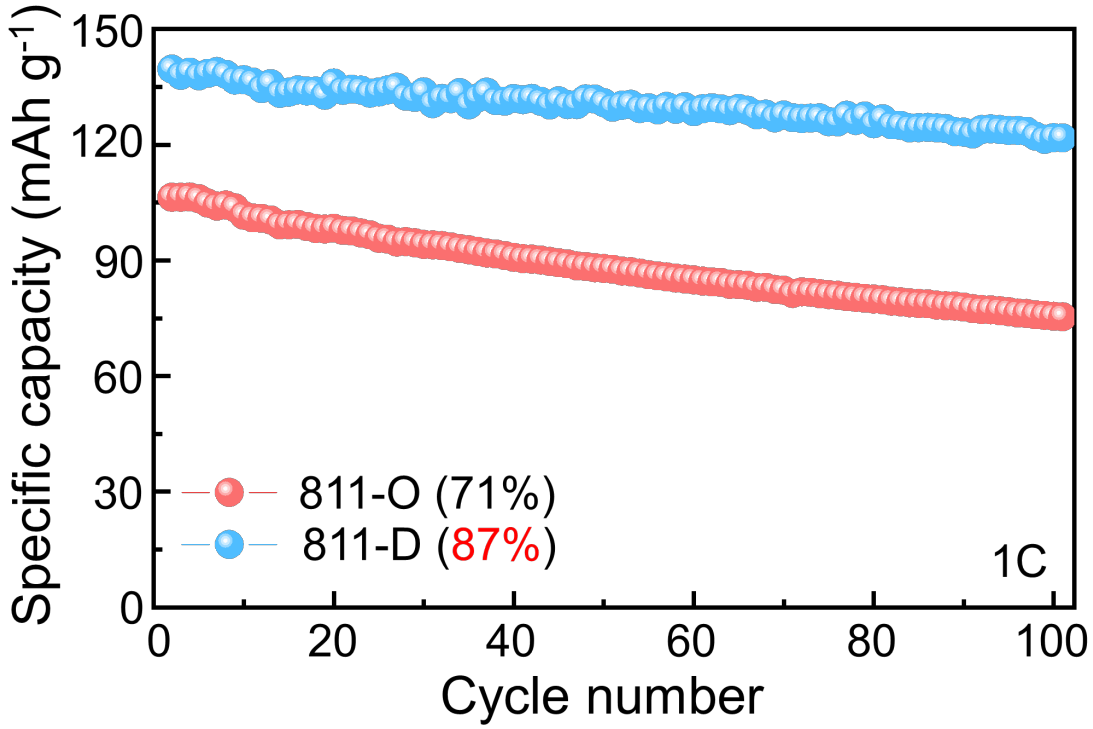

Figure S24. The long-term cycling performances of 811-O and 811-D at 1C.

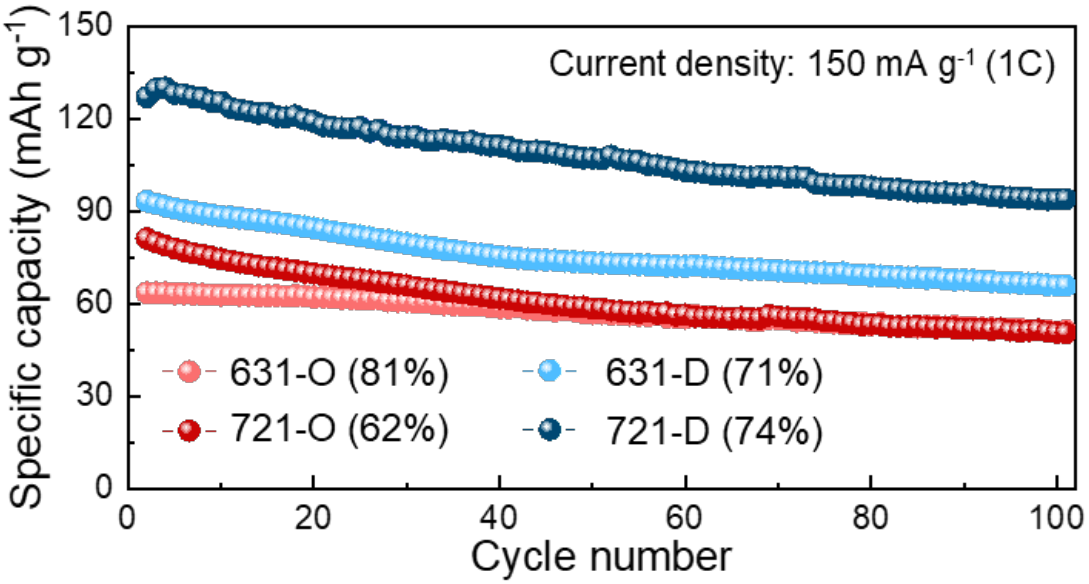

Figure S25. The long-term cycling performances of 631-O, 631-D, 721-O and 721-D at 1C.

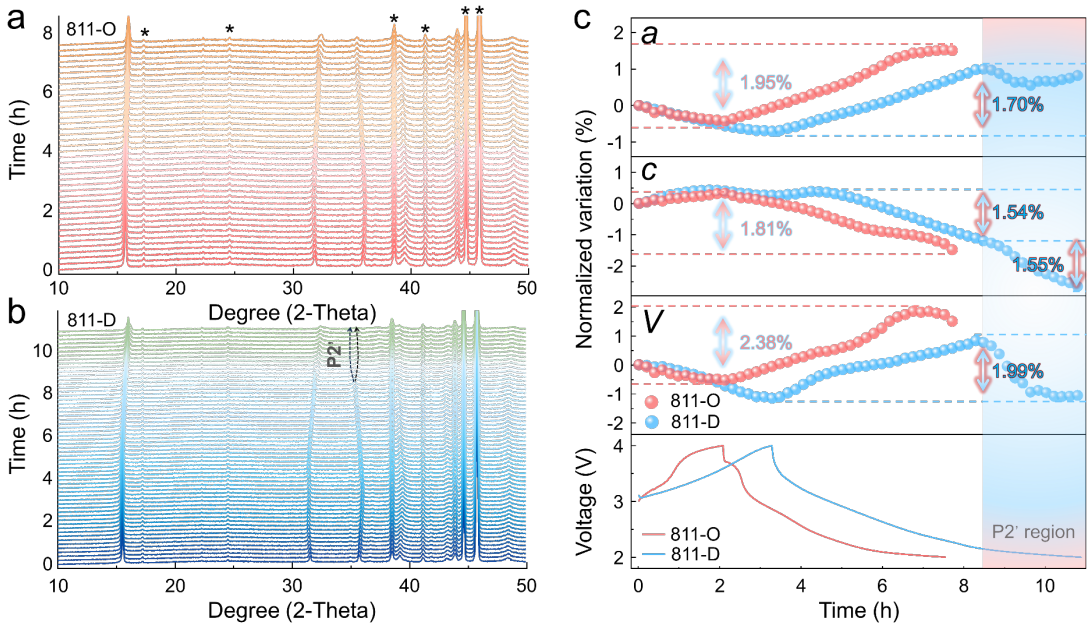

Figure S26. Structure evolution during the first electrochemical (de)sodiation processes. (a, b) *In situ* XRD patterns collected during the first charge-discharge processes of (a) 811-O and (b) 811-D at 0.15C. (c) The corresponding evolution of refined parameters (from bottom to top are lattice volume, lattice parameters *c* and *a*) during the first charging-discharging processes of 811-O and 811-D.

As shown in Figure S26a, 811-O exhibits a typical solid-solution reaction throughout the entire charge-discharge processes. Due to significant differences in insertion/extraction depths of Na^+, 811-D suffers a transition to a distorted P2' phase upon discharge to ~2.15 V.[5] However, in the deeply sodiated state, the cooperative Jahn-Teller distortion induced by Mn^{3+} ions causes severe structural deformation, which leads to interlayer cracking and ultimately results in material failure during subsequent electrochemical cycling.[5, 6] Hence, P2' phase is generally considered detrimental to structural stability, contradicting its electrochemical performance.

To further explore the specific effects of cation disorder on structural evolution, Rietveld refinements were performed on the complete set of XRD patterns for both samples. Key structural parameters from the refinement results were further extracted, such as lattice volume, *c*, and *a*. As illustrated in Figure S26c~~-S24e~~, both 811-O and 811-D display similar evolution trends during charging: an increase in *c*-axis due to the reduced Coulombic attraction between oxygen ions in adjacent transition metal layers as Na^+ is extracted, and a decrease in *a*-axis owing to the lattice contraction caused by the oxidation of cations to higher-valence states with smaller radius. Notably, for 811-D, the *c*-axis did not continuously increase during charging but

instead showed a smoother evolution at high voltages, possibly indicating structural optimization from dispersed local strain due to cation disorder. During discharging, both samples initially exhibit evolution trends opposite to those observed during charging. Until the appearance of the P2' phase in 811-D, its lattice parameters consistently show significantly lower evolution compared to 811-O. Interestingly, after the P2' phase emerges in 811-D, the *c*-axis continues its reducing trend, whereas the *a*-axis exhibits anomalous expansion. This unusual expansion of *a*-axis can be ascribed to the disruption of the Mn^{3+} cooperative Jahn-Teller distortion, facilitated by the dispersion of the distortion effect due to cation disordering.[4]

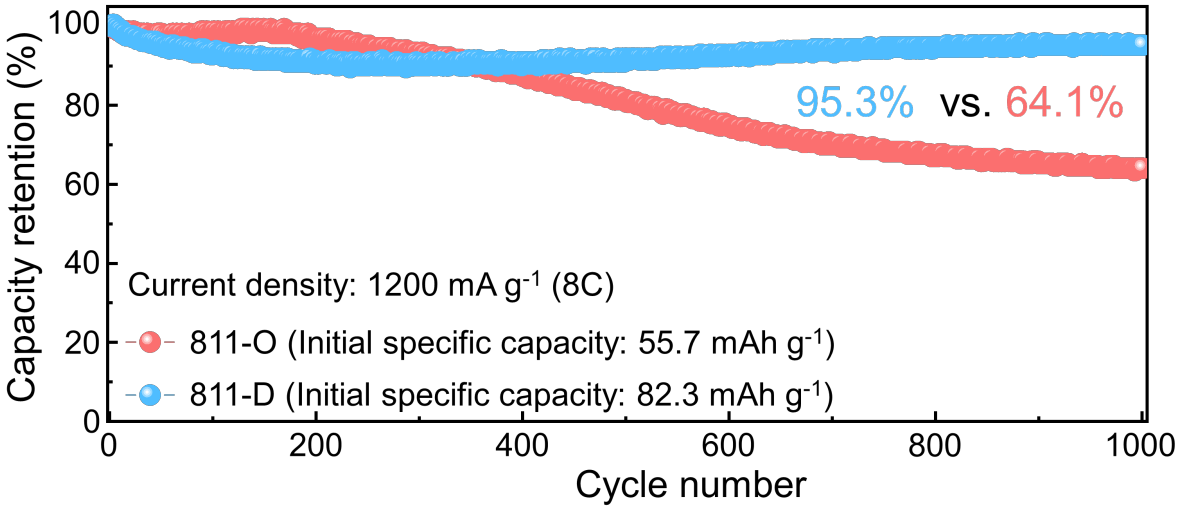

Figure S27. The long-term cycling performances of 811-O and 811-D at 8C.

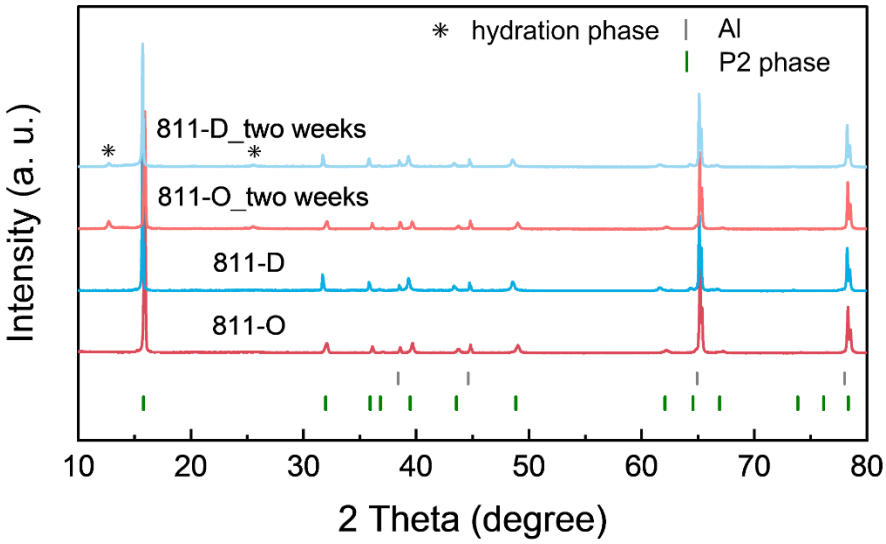

Figure S28. The air stability test of 811-O and 811-D. XRD patterns were collected from the corresponding electrodes after 0 and two weeks of air exposure.

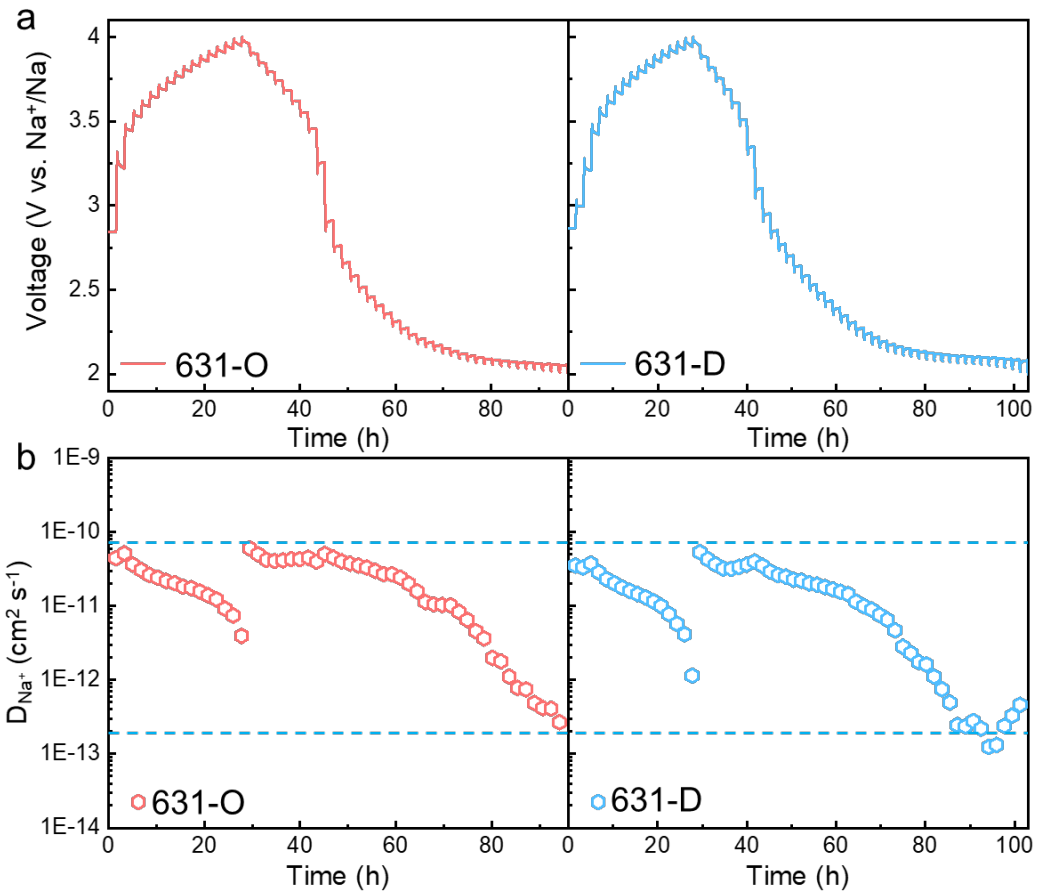

Figure S29. (a) GITT curves of 631-O and 631-D at initial cycle within 2–4 V. (b) Corresponding D_{Na^+} calculated via GITT tests.

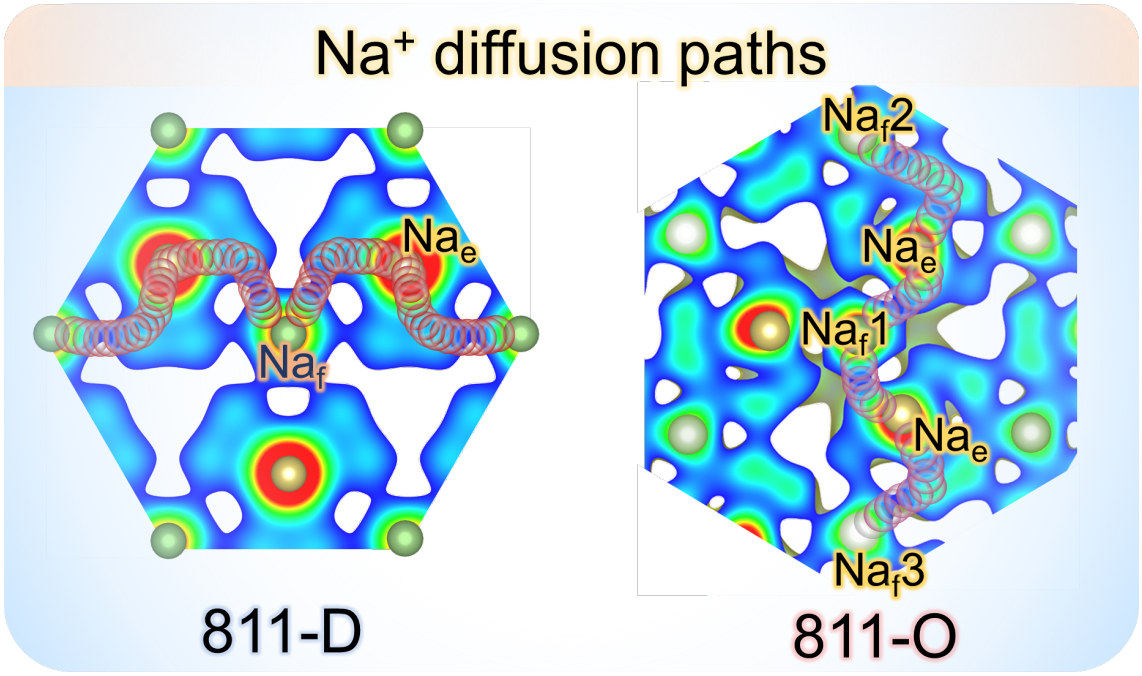

Figure S30. Na^+ diffusion pathways in both 811-D and 811-O based on MEM results and optimized DFT models.

Table S1. The Rietveld refinement result of neutron powder diffraction for 811-O.

811-O_$P6_3$						
Atom	*Wyckoff*	*x*	*y*	*z*	B_{iso} (Å^2)	*Occ.*
O	*6c1*	0.3359(3)	0.3134(8)	0.4014(6)	0.721(1)	0.9998(1)
O	*6c2*	0.6818(4)	0.6673(4)	-0.4149(4)	0.721(1)	0.9998(1)
Na_e	*6c*	0.6276(9)	0.6949(1)	0.2394(8)	3.03(2)	0.4012(8)
Na_f	*2a*	0	0	0.2394(8)	3.366(4)	0.0896(2)
Na_f	*2b*	1/3	2/3	0.2394(8)	3.366(4)	0.0896(2)
Na_f	*2b*	2/3	1/3	0.2394(8)	3.366(4)	0.0896(2)
Mn	*2a*	0	0	0	1.40(1)	0.3303(3)
Fe	*2a*	0	0	0	1.40(1)	0.0025(3)
Cu	*2a*	0	0	0	1.40(1)	0.0005(3)
Mn	*2b1*	2/3	1/3	0	1.69(2)	0.1395(6)
Fe	*2b1*	2/3	1/3	0	1.69(2)	0.0949(6)
Cu	*2b1*	2/3	1/3	0	1.69(2)	0.0990(6)
Mn	*2b2*	1/3	2/3	0	1.40(1)	0.3303(3)
Fe	*2b2*	1/3	2/3	0	1.40(1)	0.0025(3)
Cu	*2b2*	1/3	2/3	0	1.40(1)	0.0005(3)
$a = b = 4.9893(1)$ Å, $c = 11.1770(1)$ Å, $V = 240.958(4)$ Å^3, $\alpha = \beta = 90°$, $\gamma = 120°$ $R_p = 3.64\%$, $R_{wp} = 4.75\%$						

Table S2. The Rietveld refinement result of neutron powder diffraction for 721-O.

721-O_$P6_3$						
Atom	*Wyckoff*	*x*	*y*	*z*	B_{iso} (Å^2)	*Occ.*
O	*6c1*	0.3190(1)	0.3118(1)	0.3783(3)	0.717(4)	0.9993(2)
O	*6c2*	0.6849(1)	0.6575(2)	-0.4398(3)	0.717(4)	0.9993(2)
Na_e	*6c*	0.6152(8)	0.6673(8)	0.2141(7)	3.50(5)	0.3990(4)
Na_f	*2a*	0	0	0.2141(7)	1.296(6)	0.0904(1)
Na_f	*2b*	1/3	2/3	0.2141(7)	1.296(6)	0.0904(1)
Na_f	*2b*	2/3	1/3	0.2141(7)	1.296(6)	0.0904(1)
Mn	*2a*	0	0	0	1.02(3)	0.2949(1)
Fe	*2a*	0	0	0	1.02(3)	0.0381(1)
Cu	*2a*	0	0	0	1.02(3)	0.0002(1)
Mn	*2b1*	2/3	1/3	0	0.77(3)	0.1101(2)
Fe	*2b1*	2/3	1/3	0	0.77(3)	0.1237(2)
Cu	*2b1*	2/3	1/3	0	0.77(3)	0.0995(2)
Mn	*2b2*	1/3	2/3	0	1.02(3)	0.2949(1)
Fe	*2b2*	1/3	2/3	0	1.02(3)	0.0381(1)
Cu	*2b2*	1/3	2/3	0	1.02(3)	0.0002(1)
$a = b = 5.0061(1)$ Å, $c = 11.2054(3)$ Å, $V = 240.320(5)$ Å^3, $\alpha = \beta = 90°$, $\gamma = 120°$						
$R_p = 2.33\%$, $R_{wp} = 2.89\%$						

Table S3. The Rietveld refinement result of neutron powder diffraction for 631-O.

631-O_$P6_3$						
Atom	*Wyckoff*	*x*	*y*	*z*	B_{iso} (Å^2)	*Occ.*
O	*6c1*	0.3213(2)	0.3033(2)	0.3897(1)	0.548(1)	0.9987(3)
O	*6c2*	0.6709(3)	0.6618(3)	-0.4294(1)	0.548(1)	0.9987(3)
Na_e	*6c*	0.6010(7)	0.6421(3)	0.2453(3)	3.46(2)	0.4095(7)
Na_f	*2a*	0	0	0.2453(3)	1.970(6)	0.0857(2)
Na_f	*2b*	1/3	2/3	0.2453(3)	1.970(6)	0.0857(2)
Na_f	*2b*	2/3	1/3	0.2453(3)	1.970(6)	0.0857(2)
Mn	*2a*	0	0	0	0.24(1)	0.2266(1)
Fe	*2a*	0	0	0	0.24(1)	0.0999(1)
Cu	*2a*	0	0	0	0.24(1)	0.0066(1)
Mn	*2b1*	2/3	1/3	0	0.24(2)	0.1466(2)
Fe	*2b1*	2/3	1/3	0	0.24(2)	0.1000(2)
Cu	*2b1*	2/3	1/3	0	0.24(2)	0.0866(2)
Mn	*2b2*	1/3	2/3	0	0.24(1)	0.2266(1)
Fe	*2b2*	1/3	2/3	0	0.24(1)	0.0999(1)
Cu	*2b2*	1/3	2/3	0	0.24(1)	0.0066(1)
$a = b = 5.0291(1)$ Å, $c = 11.2263(1)$ Å, $V = 245.892(8)$ Å^3, $\alpha = \beta = 90°$, $\gamma = 120°$ $R_p = 2.00\%$, $R_{wp} = 2.46\%$						

Table S4. The Rietveld refinement result of neutron powder diffraction for 811-D.

811-D_$P6_3/mmc$						
Atom	*Wyckoff*	*x*	*y*	*z*	B_{iso} (Å^2)	*Occ.*
O	*4f*	1/3	2/3	0.40848(3)	1.418(5)	0.9864(3)
Na_e	*2d*	1/3	2/3	3/4	3.52(3)	0.4171(2)
Na_f	*2b*	0	0	1/4	3.17(3)	0.2495(2)
Mn	*2a*	0	0	0	1.01(3)	1/3
Fe	*2a*	0	0	0	1.01(3)	1/3
Cu	*2a*	0	0	0	1.01(3)	1/3
$a = b = 2.9014(1)$ Å, $c = 11.2112(2)$ Å, $V = 81.733(2)$ Å^3, $\alpha = \beta = 90°$, $\gamma = 120°$ $R_p = 2.78\%$, $R_{wp} = 3.52\%$						

Table S5. The Rietveld refinement result of neutron powder diffraction for 721-D.

721-D_$P6_3$						
Atom	*Wyckoff*	*x*	*y*	*z*	B_{iso} (Å^2)	*Occ.*
O	*6c1*	0.3344(4)	0.3385(4)	0.4028(1)	1.127(2)	0.9969(7)
O	*6c2*	0.6869(2)	0.6722(2)	-0.4132(1)	1.127(2)	0.9969(7)
Na_e	*6c*	0.6328(8)	0.7082(9)	0.2398(7)	3.56(5)	0.4567(6)
Na_f	*2a*	0	0	0.2398(7)	0.678(5)	0.0699(2)
Na_f	*2b*	1/3	2/3	0.2398(7)	0.678(5)	0.0699(2)
Na_f	*2b*	2/3	1/3	0.2398(7)	0.678(5)	0.0699(2)
Mn	*2a*	0	0	0	1.12(3)	0.2418(2)
Fe	*2a*	0	0	0	1.12(3)	0.0667(2)
Cu	*2a*	0	0	0	1.12(3)	0.0248(2)
Mn	*2b1*	2/3	1/3	0	0.80(3)	0.2163(4)
Fe	*2b1*	2/3	1/3	0	0.80(3)	0.0668(4)
Cu	*2b1*	2/3	1/3	0	0.80(3)	0.0503(4)
Mn	*2b2*	1/3	2/3	0	1.12(3)	0.2418(2)
Fe	*2b2*	1/3	2/3	0	1.12(3)	0.0667(2)
Cu	*2b2*	1/3	2/3	0	1.12(3)	0.0248(2)
$a = b = 5.0525(1)$ Å, $c = 11.1925(2)$ Å, $V = 247.444(4)$ Å^3, $\alpha = \beta = 90°$, $\gamma = 120°$						
$R_p = 1.52\%$, $R_{wp} = 2.07\%$						

Table S6. The Rietveld refinement result of neutron powder diffraction for 631-D.

631-D_$P6_3$						
Atom	*Wyckoff*	*x*	*y*	*z*	B_{iso} (Å^2)	*Occ.*
O	*6c1*	0.3331(5)	0.3192(5)	0.3873(1)	0.762(2)	0.9985(3)
O	*6c2*	0.6626(4)	0.6597(4)	-0.4317(1)	0.762(2)	0.9985(3)
Na_e	*6c*	0.7325(9)	0.7076(7)	0.2443(3)	1.84(2)	0.4294(4)
Na_f	*2a*	0	0	0.2443(3)	1.609(6)	0.0791(1)
Na_f	*2b*	1/3	2/3	0.2443(3)	1.609(6)	0.0791(1)
Na_f	*2b*	2/3	1/3	0.2443(3)	1.609(6)	0.0791(1)
Mn	*2a*	0	0	0	0.69(3)	0.2128(1)
Fe	*2a*	0	0	0	0.69(3)	0.0999(1)
Cu	*2a*	0	0	0	0.69(3)	0.0206(1)
Mn	*2b1*	2/3	1/3	0	0.73(4)	0.1744(2)
Fe	*2b1*	2/3	1/3	0	0.73(4)	0.1000(2)
Cu	*2b1*	2/3	1/3	0	0.73(4)	0.0589(2)
Mn	*2b2*	1/3	2/3	0	0.69(3)	0.2128(1)
Fe	*2b2*	1/3	2/3	0	0.69(3)	0.0999(1)
Cu	*2b2*	1/3	2/3	0	0.69(3)	0.0206(1)

$a = b = 5.0611(1)$ Å, $c = 11.1909(2)$ Å, $V = 248.244(8)$ Å^3, $\alpha = \beta = 90°$, $\gamma = 120°$

$R_p = 1.68\%$, $R_{wp} = 2.17\%$

Table S7. Stoichiometric elemental indices based on the ICP-OES measurements

Sample	Na	Mn	Fe	Cu	Formula
811-O	0.67	0.791	0.110	0.099	$Na_{0.67}Mn_{0.791}Fe_{0.110}Cu_{0.099}$
811-D	0.66	0.797	0.103	0.100	$Na_{0.66}Mn_{0.797}Fe_{0.103}Cu_{0.100}$

References

[1] a) J. M. Paulsen, J. R. Dahn, *Solid State Ionics* **1999**, 126, 3; b) L. F. Pfeiffer, N. Jobst, C. Gauckler, M. Lindén, M. Marinaro, S. Passerini, M. Wohlfahrt-Mehrens, P. Axmann, *Electrochemistry and Influence of Ambient Storage* **2022**, 10.

[2] S. Kumakura, Y. Tahara, K. Kubota, K. Chihara, S. Komaba, *Angewandte Chemie-International Edition* **2016**, 55, 12760.

[3] J. W. Somerville, A. Sobkowiak, N. Tapia-Ruiz, J. Billaud, J. G. Lozano, R. A. House, L. C. Gallington, T. Ericsson, L. Häggström, M. R. Roberts, U. Maitra, P. G. Bruce, *Energy & Environmental Science* **2019**, 12, 2223.

[4] J. Jin, Y. Liu, X. Zhao, H. Liu, S. Deng, Q. Shen, Y. Hou, H. Qi, X. Xing, L. Jiao, J. Chen, *Angewandte Chemie-International Edition* **2023**, 62, e202219230.

[5] S. Kumakura, Y. Tahara, K. Kubota, K. Chihara, S. Kom*aba, Angewandte Chemie-International Edition* **2016**, 55, 12760.

[6] R. Stoyanova, D. Carlier, M. Sendova-Vassileva, M. Yoncheva, E. Zhecheva, D. Nihtianova, C. Delmas, *Journal of Solid State Chemistry* **2010**, 183, 1372